SCIENTIFIC REPORTS

Visualizing Brain Inflammation with a Shingled-Leg Radio-Frequency Head Probe for ^{19}F/^{1}H MRI

Helmar Waiczies[1,2], Stefano Lepore[1,2], Susanne Drechsler[1,2], Fatimunnisa Qadri[2,3], Bettina Purfürst[4], Karl Sydow[5], Margitta Dathe[5], André Kühne[6], Tomasz Lindel[6], Werner Hoffmann[6], Andreas Pohlmann[1], Thoralf Niendorf[1,2] & Sonia Waiczies[1,2]

[1]Berlin Ultrahigh Field Facility (B.U.F.F.), Max Delbrück Center for Molecular Medicine, [2]Experimental and Clinical Research Center, a joint cooperation between the Charité Medical Faculty and the Max Delbrück Center for Molecular Medicine, [3]Molecular Biology of Peptide Hormones, Max Delbrück Center for Molecular Medicine, [4]Electron Microscopy Core Facility, Max Delbrück Center for Molecular Medicine, [5]Peptide Lipid Interaction/Peptide Transport, Leibniz-Institut für Molekulare Pharmakologie (FMP), [6]Department of Medical Physics and Metrological Information Technology, Physikalisch Technische Bundesanstalt (PTB).

Magnetic resonance imaging (MRI) provides the opportunity of tracking cells *in vivo*. Major challenges in dissecting cells from the recipient tissue and signal sensitivity constraints albeit exist. In this study, we aimed to tackle these limitations in order to study inflammation in autoimmune encephalomyelitis. We constructed a very small dual-tunable radio frequency (RF) birdcage probe tailored for ^{19}F (fluorine) and ^{1}H (proton) MR mouse neuroimaging. The novel design eliminated the need for extra electrical components on the probe structure and afforded a uniform B_1^+-field as well as good SNR. We employed fluorescently-tagged ^{19}F nanoparticles and could study the dynamics of inflammatory cells between CNS and lymphatic system during development of encephalomyelitis, even within regions of the brain that are otherwise not easily visualized by conventional probes. ^{19}F/^{1}H MR Neuroimaging will allow us to study the nature of immune cell infiltration during brain inflammation over an extensive period of time.

Inflammation is a key player in several disorders of the central nervous system (CNS). In autoimmune encephalomyelitis a recruitment of immune cells to the CNS occurs early during the pathogenesis, prior to the onset of neurological symptoms[1–3]. The tracking of immune cells into the brain and spinal cord is thus pivotal for understanding the development of CNS inflammation in preclinical animal models such as experimental autoimmune encephalomyelitis (EAE). Strategies for following cells in the CNS during EAE have commonly made use of iron oxide nanoparticles that reduce T2* relaxation[4–7]. One drawback of these contrast agents is the difficulty to distinguish the negative contrast created by the labeled cells from other intrinsic tissue contrasts. This, together with the lack of an *a priori* knowledge of the kinetics of immune cell migration during inflammation, makes the localization of immune cells in the CNS a challenging task. The use of fluorine (^{19}F)-rich nanoparticles to track inflammatory cells, in conjunction with ^{19}F/^{1}H MRI, is an emerging approach for cell tracking[8]. Due to the absence of organic ^{19}F *in vivo*, ^{19}F/^{1}H MRI is advantageous for localizing transplanted cells *in vivo* since it permits background-free images with complete signal selectivity and specificity. The possibility of quantifying the cell signal by ^{19}F MR spectroscopy is another advantage.

One major limitation when tracking immune cells in the CNS with ^{19}F/^{1}H MRI is the low signal-to-noise ratio (SNR) for both ^{19}F and ^{1}H signals. The SNR and the sensitivity of the radio frequency (RF) probe used are indeed main determinants that dictate the level of spatial resolution[9]. Factors to be kept in mind when designing a probe include the geometry, the filling factor and the homogeneity of the B_1^+-transmit field. Small-sized birdcage probes are ideal for mouse neuroimaging but are quite challenging to build due to size and increased risk of inaccurate assembly of chip capacitors that could distort the circuit symmetry and RF homogeneity. The millipede design was developed to eliminate the necessity of chip capacitors[10]. However millipede probes are too complex to be modified as double-tunable probes; an assembly of two spiral coils would need to be constructed to achieve a double resonant setup[10] but this results in an undesirable sensitivity difference between outer and inner coils. In order to track inflammatory cells *in vivo* with ^{19}F/^{1}H MRI, a dual-tunable RF probe is desirable in order to

safeguard sensitivity and B_1-field homogeneity on both frequencies and to avoid inaccurate co-registration of both signals[11].

In this study we constructed a novel dual-tunable $^{19}F/^{1}H$ birdcage probe with a shingled-leg design in order to detect immune cell infiltration in the mouse brain during encephalomyelitis. Thirty two copper strips were arranged in parallel to form a cylinder and overlapped with strips extending from the end rings of the RF probe. This provided plate capacitance on each leg, thereby eliminating the necessity of solid chip capacitors. With our RF probe we were able to detect inflammatory cell infiltrates as ^{19}F signal in EAE mice following *in vivo* administration of fluorescently-labeled ^{19}F-rich particles. We observed immune cell penetration even in regions of the CNS e.g. anterior region of brainstem and spinal cord that are otherwise not easily visualized by conventional RF probes due to limited depth penetration.

Results

Electromagnetic field simulations and performance of the RF head. We first performed simulations with a finite integration technique (MWS) using a shield diameter of 58 mm and determined that we require a capacitance of 1.14 pF in order to tune to 400 MHz (^{1}H frequency at 9.4 Tesla). These results were in close agreement with those calculated using an analytical method (Birdcage Builder), in which we determined a required capacitance of 1.17 pF ($<3\%$ deviation). Since the calculated capacitor values were small (**Figure 1**) and considering the need for accuracy, especially in the increments between the capacitors, we decided to circumvent conventional chip capacitors during construction of the birdcage. Instead we introduced a shingled birdcage design, in which capacitors were built, with high accuracy, into the structure of the RF probe. For this the copper milling on either side of the PCB was done
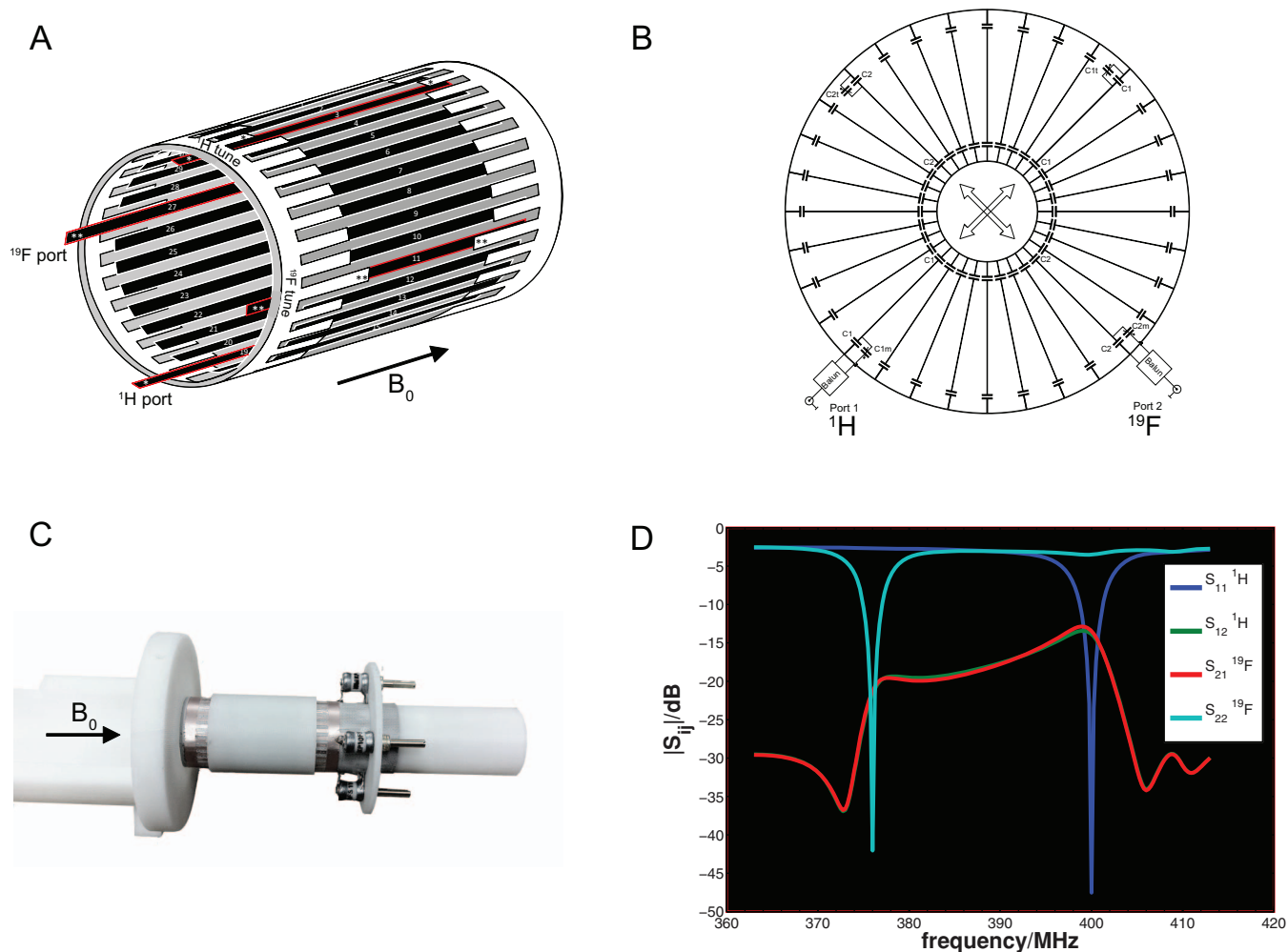

Figure 1 | Design and Construction of the $^{19}F/^{1}H$ RF Birdcage Mouse Head Probe. (A) Sketch of the 32 leg low-pass birdcage probe shows the main setup consisting of long copper strip-lines (shown in black) that overlap with the peripheral copper strip-lines (shown in white) connected together by the end rings. Out of 32 legs, 28 copper-strips were uniformly overlapped by an area of 6.27 mm² to achieve a center frequency of 388 MHz, 2 strip-lines (marked with *) overlapped by a smaller area (3.14 mm²) to tune for ^{1}H at 400 MHz (for 9.4 Tesla) and 2 strip-lines (marked with **) overlapped by an area of 9.39 mm² to tune for ^{19}F at 376 MHz (for 9.4 Tesla). The probe axis is aligned with the direction of the static magnetic field B_o. (B) Circuit diagram of the birdcage probe showing the 56 capacitors ($C_{legs} = 1.38$ pF, resulting from the above uniformly overlapped 28 legs) that adjust the birdcage to the center frequency (388.35 MHz), C1 (0.69 pF) capacitors (created by the 2 legs with 3.14 mm² overlap) that tune one port to ^{1}H mode and C2 (2.08 pF) capacitors (created by the 2 legs with 9.39 mm² overlap) that tune the other port to ^{19}F mode. C1m/C2m are the matching capacitors and C1t/C2t the tuning capacitors in the range of 1–6 pF. (C) Photograph of the constructed birdcage (without shield) in correct alignment with the direction of the static magnetic field B_o. Arrow also indicates the access point and direction of the prone-positioned mouse for head imaging. (D) Examination of RF performance with respect to the scattering (S) parameters shows that port 1 (^{1}H) resonates at 400 MHz and Port 2 (^{19}F) at 376 MHz. The reflection coefficients on both ports (S_{11} and S_{22}) are shown to be lower than -40 dB and the coupling between the ports (S_{12} and S_{21}) is shown to be lower than -15 dB.

in a way to create an overlap between the inner and outer copper strips, thereby creating plate capacitors along the length of the birdcage legs (**Figure 1A–1C**). To fine tune to the exact ^{1}H (400 MHz) and ^{19}F (376 MHz) frequencies required at 9.4 Tesla, the shield diameter was reduced from 58 mm (used for the first simulations) to 48 mm. This shield diameter was used for the construction of the coil design as well as for the final EMF simulations. Based on the required capacitance results calculated from MWS and the Birdcage Builder, an overlap of 6.27 mm^2 (equivalent to 1.38 pF) was used for the simulation (**Figure 2A–2D**) and ultimate construction (**Figure 1C**) in order for the birdcage to resonate at a main frequency of 388 MHz that is approximately half way between ^{1}H and ^{19}F when calculating the square root of the product of both frequencies ($\sqrt{400 * 376} = 387.81$ MHz).

Upon evaluation of the B_1^+ profiles in the EMF simulations for this setup (**Figure 2A**), we observed high B_1^+ homogeneity throughout the whole birdcage probe for both ^{1}H and ^{19}F modes (**Figure 2B and Supplementary Figure 1**). However, EMF simulations (particularly B_1^+ distribution) are only an estimation for a given setup, which does not take power losses into consideration. We therefore compared the B_1^+ field values achieved from the EMF simulation with real B_1^+ field values measured with the constructed birdcage probe in a 9.4 Tesla animal scanner for the ^{1}H channel (**Figure 2C**). For both simulation and measurement experiments, the same input power and absorbed tissue power in the phantom were employed (ignoring powers losses in cables, plugs and baluns). We calculated a maximum B_1^+ profile of 40 $\mu T/\sqrt{W}$ for the simulations and 31 $\mu T/\sqrt{W}$ for the measurement at the center of the slice (**Figure 2C, 2D**). The B_1^+ profile over the cross-section of the cylindrical phantom ranged from 38–40 $\mu T/\sqrt{W}$ for the measurement and 29–31 $\mu T/\sqrt{W}$ for the simulation (**Figure 2D**). The factor of 1.66 between B_1^+ simulations and B_1^+ measurements translates to a power attenuation of about 2.2 dB.

This power attenuation is in agreement with losses in the RF chain (from amplifier to probe) that we could estimate from the properties of the cable and using the network analyzer.

Owing to the shingled design of the birdcage with variable overlaps between the copper strips, the RF probe could be tuned to both ^{1}H and ^{19}F frequencies. With this setup, the reflection coefficients (S_{11} and S_{22}) were below -40 dB for both frequencies (**Figure 1D**). The transmission coefficients (S_{12} and S_{21}) determine the extent of power lost via transmission between the 2 ports and was below -15 dB thereby not necessitating additional decoupling capacitors. Using the reflection coefficients we could measure the RF probe/coil quality as QFactor. This determines the extent of noise contribution coming from the RF probe or sample. We thus measured the QFactor of both loaded (Q_L) and unloaded (Q_U) RF probe using the formula "$Q = f_r/BW$" where f_r is the specific resonance frequency (400 MHz for ^{1}H) and BW is the corresponding bandwidth frequency at half maximum peak. We calculated Q_U to be 130. Q_L was calculated to be 80–110, depending on the load of the probe, the size of the mouse or conductivity of the phantom). For 376 MHz (^{19}F), Q-values were similar ($Q_U \approx 150$).

^{19}F/^{1}H MR tracking of cell infiltrates in experimental autoimmune encephalomyelitis (EAE).

We performed ^{19}F/^{1}H MR imaging and spectroscopy of EAE mouse brains using the constructed head birdcage ^{19}F/^{1}H RF probe. For the first set of experiments (**Figure 3**) we induced EAE in SJL/J mice and administered ^{19}F-rich nanoparticles (Z-Average Diam. = 160 nm) intravenously in these mice only upon the first signs of neurological symptoms. Using the constructed ^{19}F/^{1}H RF probe and a 2D T_2-weighted gradient echo (FLASH) sequence for ^{1}H MRI, we observed hypointense lesions as previously reported[12] in the cerebellum (**Figure 3A, 3C**) and cerebral cortex (**Figure 3D, 3F**) of sick mice. In these experiments we decided
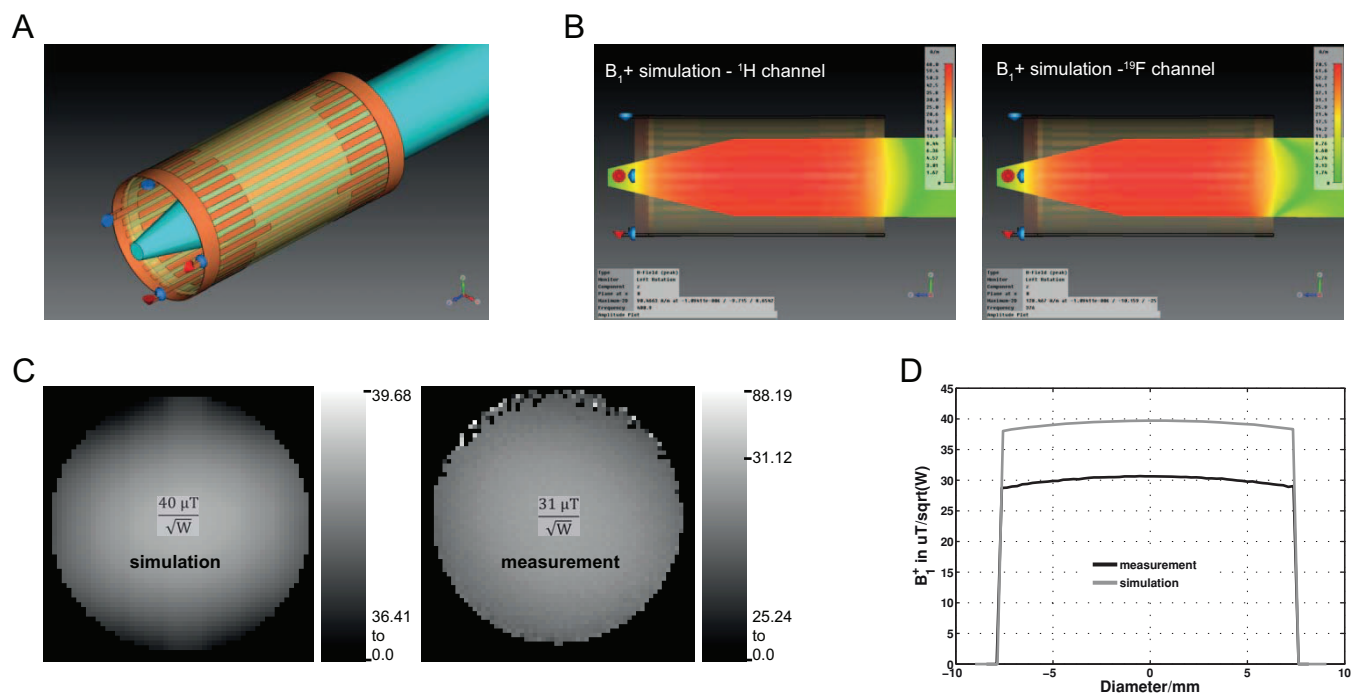

Figure 2 | B_1^+-Field Distribution for the ^{19}F/^{1}H RF Birdcage Probe. (A) Three dimensional design of the ^{19}F/^{1}H RF birdcage probe holding a phantom (turquoise) simulated with a finite integration technique (CST Studio Suite). For the measurements a phantom with similar dielectric properties and geometry was used. (B) Sagittal cross-section through the simulated B_1^+-field within the phantom. (C) Comparison of B_1^+-field measurement of the ^{1}H channel with the simulation of a central slice, scaled to the same input power and absorbed tissue-power in the object, not considering cable losses, plugs and baluns. (D) Shows a line-plot through the center of the simulated and measured B_1^+-field, with a maximum of 40 $\mu T/\sqrt{W}$ in the simulation and 31 $\mu T/\sqrt{W}$ for the measurement at the center. B_1^+-profile over the center slice ranges from 38–40 $\mu T/\sqrt{W}$ in the simulation and 29–31 $\mu T/\sqrt{W}$ in the measurement.

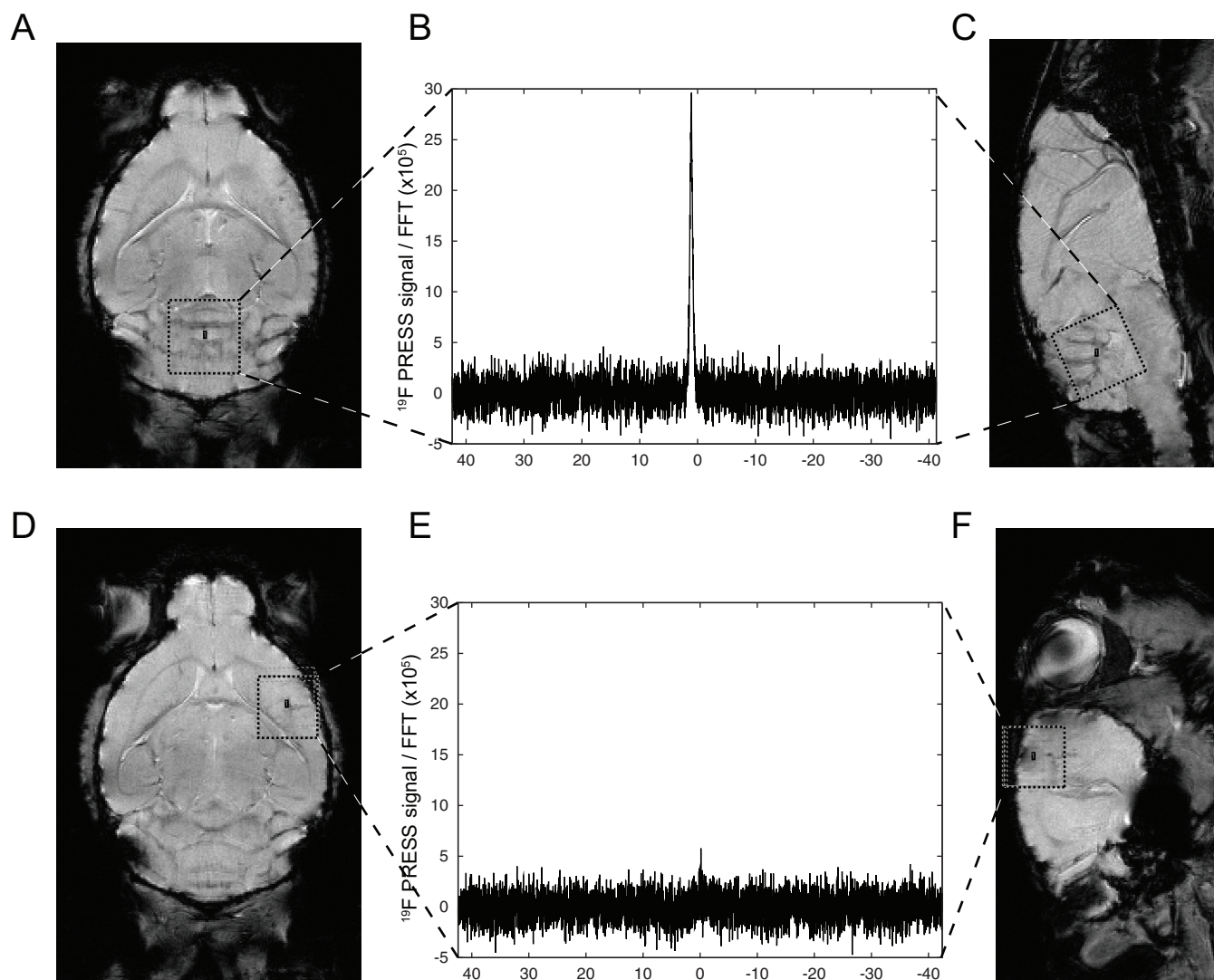**Figure 3 | In Vivo ¹⁹F Quantification in an EAE mouse Brain using Single Voxel ¹⁹F Spectroscopy.** EAE was induced in SJL/J mice and 160 nm ¹⁹F-rich nanoparticles (40 μmoles ¹⁹F) were administered on the first signs of neurological symptoms. (A) Horizontal and (C) sagittal slices identifying lesions in the cerebellum; dotted box depicts the location of the 3 mm³ PRESS voxel around the lesion of interest within the cerebellum. (B) ¹⁹F MRS spectrum of the PRESS voxel in the cerebellum. (D) Horizontal and (F) sagittal slices identifying lesions in the cortex; dotted box depicts the location of the 3 mm³ PRESS voxel around the hypointense lesion within the cortex. (E) ¹⁹F MRS spectrum of the PRESS voxel in the cortex.

to administer one single shot of ¹⁹F-rich nanoparticles with high ¹⁹F content (corresponding to 40 μmoles) at the start of disease. Following 24 hours of nanoparticle application, we performed ¹⁹F PRESS to determine the ¹⁹F signal in the regions where we could detect hypointense lesions. For this, we localized a 3 mm³ PRESS voxel around the cerebellum (**Figure 3A, 3C**) and another PRESS voxel around the hypointense lesion within the cortex (**Figure 3D, 3F**). In contrast to the selected region within the cortex (**Figure 3E**), we could detect a strong ¹⁹F signal in the PRESS voxel in the cerebellum (**Figure 3B**), where we also observed larger areas of anatomical alterations using the ¹H gradient echo sequence (**Figure 3A**). With the help of a calibration measurement we calculated the ¹⁹F content within the cerebellum to be c. 60 nmoles.

Next, we wanted to determine the location of the ¹⁹F signal distributed within the cerebellum using ¹⁹F/¹H MRI. To do so, we selected a 3 mm sagittal slice through the brain (**Figure 4A**), which encloses the 3 mm³ PRESS voxel, and acquired ¹⁹F gradient echo (FLASH) images. When we overlaid the T₂-weighted ¹H image (in-plane spatial resolution (73 × 73) μm²) of the median sagittal slice (**Figure 4B**) with the ¹⁹F image (**Figure 4C**) of the same sagittal section we observed co-localization of the ¹⁹F signal to the brain stem

and mostly the cerebellum, particularly in the white matter (**Figure 4D**). Following these ¹⁹F/¹H MRI measurements we extracted the brain and prepared the cerebellum for electron microscopy. Already with the help of Differential Interference Contrast microscopy, we observed small, round and white particles engulfed within macrophage-like cells that were infiltrating the cerebellar lesions (**Figure 4E**). Electron microscopy revealed these particles as bright smooth spheroids clustered within phagosomes in the cytoplasm of macrophage-like cells (**Fig 4F–4H**).

Considering the highly homogeneous field provided by our MR head probe, we decided to implement accelerated spin echo techniques that are otherwise very sensitive to fluctuations in the B_1^+ field[13,14]. Apart from altering the scanning method, we also changed the protocol of systemic ¹⁹F nanoparticle administration. We injected nanoparticles (same particle size but 5 μmoles ¹⁹F content) daily, starting from day 5 following immunization. The first MRI measurements were performed on the first day of symptoms. First we acquired an *in vivo* ¹H 3D TurboRARE sequence using a standard protocol (TR = 1500 ms, TE = 53 ms, FOV = (40 × 16 × 16) mm³, Matrix = 320 × 128 × 128, RARE Factor = 16, NEX = 1 (scan time = 25 min) to achieve a T₂-weighted image with an isotropic resolu-
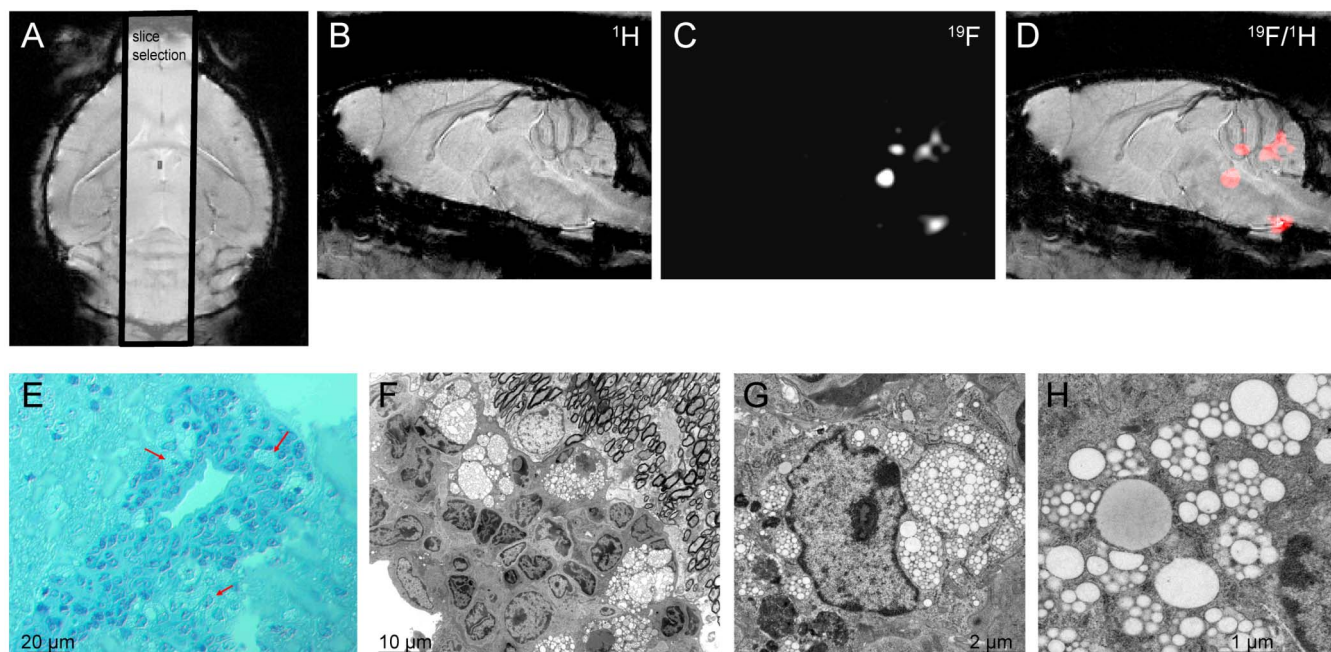
Figure 4 | ¹⁹F/¹H MRI and Electron Microscopy of the ¹⁹F-rich Particles within the Cerebellum of an EAE Mouse Brain. (A) Horizontal slice of the previous SJL/J mouse-brain using 2D-FLASH imaging: TR = 473 ms, TE = 13 ms, 22 slices, in-plane resolution 73 μm², NEX = 16 (scan time = 25 min). The black outlined box depicts the slice selection for the ¹⁹F acquisition. (B) Median sagittal slice of the same mouse brain. (C) ¹⁹F image of the 3 mm central slice using 2D FLASH TR = 15 ms, TE = 3.3 ms, 1 3 mm slice, in-plane resolution (400 × 400) μm², NEX = 2048 (scan time = 15 min) and (D) an overlay of (C) (in gray) and (D) (in red). (E) to (H) Histological slices of the extracted cerebellum. (E) Differential interference contrast image of a cerebellar lesion (toluidine blue staining) which shows small round and white nanoparticles engulfed into macrophage like cell structures (red arrows). (F) to (H) high resolution electron microscopy images of adjacent regions.

tion of 125 μm³. Following this, we performed a ¹⁹F MR TurboRARE sequence in the same mouse after it had undergone terminal anesthesia. For this, we employed the following ¹⁹F MR protocol: TR = 1000 ms, TE = 6 ms, scan time = 690 min, FOV = (40 × 16 × 16) mm³, Matrix = 100 × 40 × 40, zero fill acceleration = 2, RARE Factor = 40, NEX = 2048, leading to a reconstructed isotropic resolution of 400 μm³. When we overlaid the acquired ¹⁹F scans with the previous ¹H images, we observed that areas of inflammatory cell involvement were mostly within the spinal cord, brain stem, cerebellum and cerebral cortex (also in close proximity to the ventricles) as shown in horizontal (**Figure 5A**) and sagittal (**Figure 5B**) serial images of the brain. We also detected a strong ¹⁹F signal within the cervical draining lymph nodes, areas of expected high inflammatory cell activity. These scans were the first to reveal the uptake of ¹⁹F nanoparticles by immune cells and their extensive infiltration of these cells throughout the CNS and secondary lymphatic organs as shown by ¹⁹F MRI.

In order to follow the dynamics of inflammatory cells during EAE *in vivo*, we altered the above ¹⁹F MR protocol to reduce the acquisition time to 68 min. Following acquisition of the above ¹H 3D TurboRARE sequence, we performed an *in vivo* ¹⁹F MRI using the following protocol: TR = 800 ms, TE = 6 ms, FOV = (40 × 16 × 16) mm³, Matrix = 100 × 40 × 40, zero fill acceleration 2, RARE Factor = 40, NEX = 256. Similarly to the longer ¹⁹F scans in the previous *ex vivo* experiments, the ¹⁹F signals that we detected *in vivo* were mostly located within draining lymph nodes, the spinal cord, brain stem, cerebellum and cerebral cortex (**Figure 6A**). Typically, the draining lymph nodes were the first to give a ¹⁹F signal (between day 5 and day 8); the ¹⁹F signal extended from the submandibular and superficial cervical lymph nodes into the deeper cervical, facial and internal jugular lymph nodes. Between day 8 and day 11 we observed immune cell infiltration in the CNS.
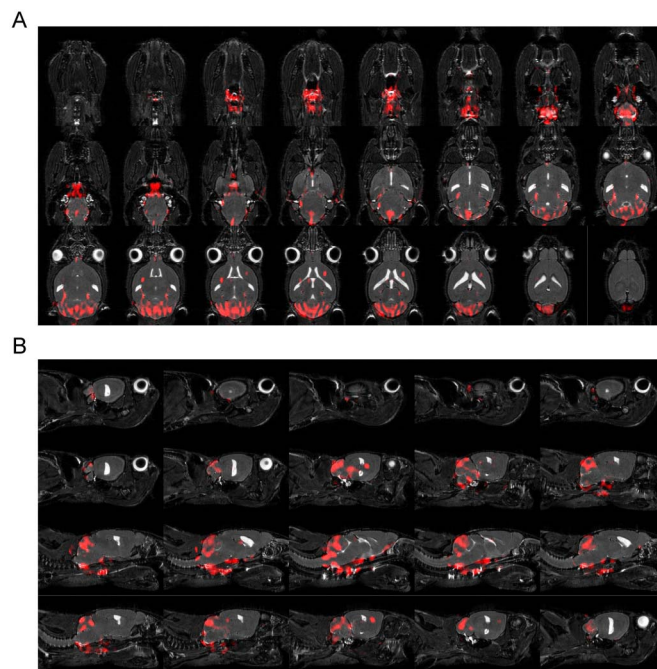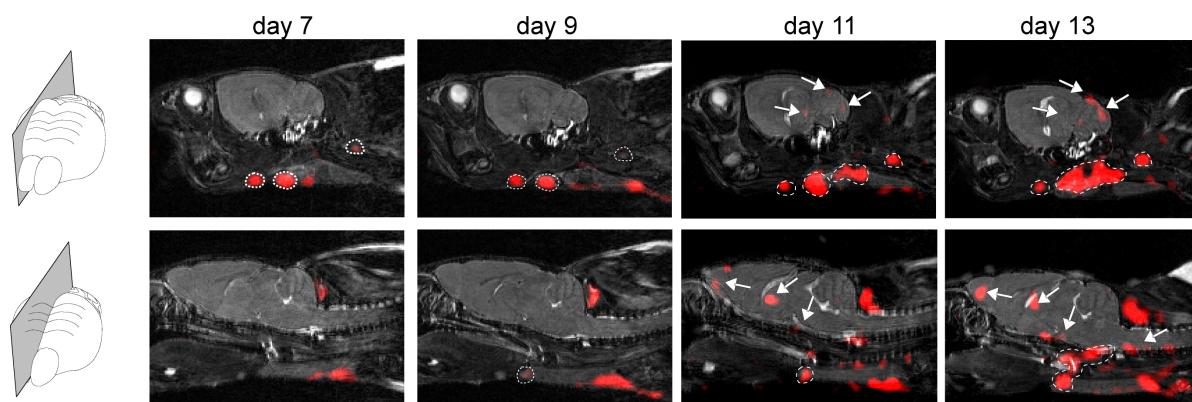

Figure 5 | In Vivo ¹H (grey) and Post Mortem ¹⁹F MR(red) Images. EAE was induced in SJL/J mice and 160 nm ¹⁹F-rich nanoparticles (5 μmoles ¹⁹F) were administered daily, starting from day 5 following immunization.(A) Horizontal and (B) sagittal slices of a 3D TurboRARE-scan for *in vivo* ¹H (grayscale): TR = 1500 ms, TE = 53 ms, FOV = (40 × 16 × 16) mm³, Matrix = 320 × 128 × 128, RARE Factor = 16, NEX = 1 (scan time = 25 min) and for *ex vivo* ¹⁹F (red): TR = 1000 ms, TE = 6 ms, FOV = (40 × 16 × 16) mm³, Matrix = 100 × 40 × 40, zero fill acceleration 2, RARE Factor = 40, NEX = 2048 (scan time = 690 min).
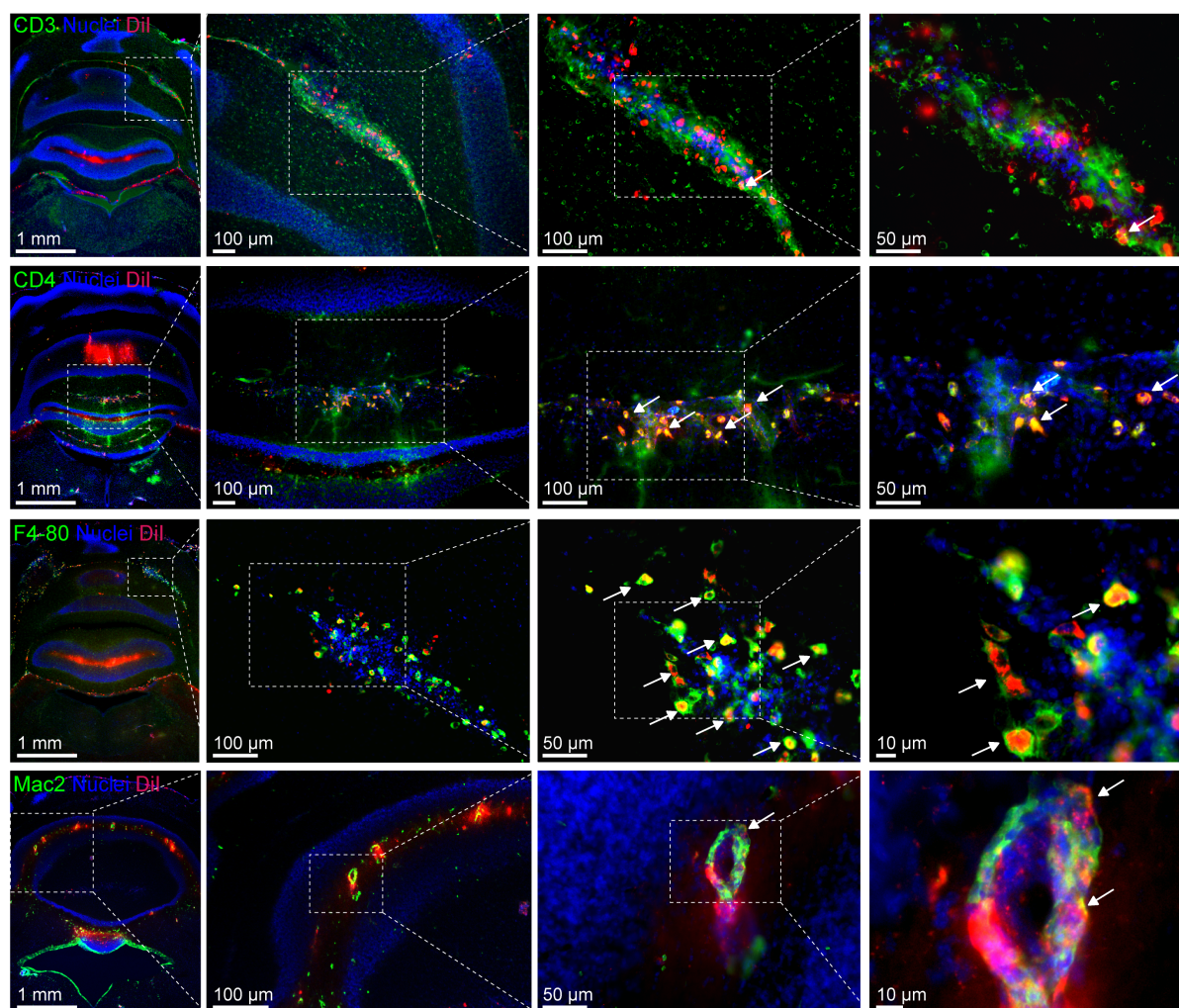
Figure 6 | Visualization of Inflammatory Cells in different CNS and Lymphatic Regions using In Vivo ^{19}F/ ^{1}H MRI. EAE was induced in SJL/J mice and 170 nm ^{19}F-rich and DiI-labeled nanoparticles (5 µmoles ^{19}F) were administered daily, starting from day 5 following immunization. (A) Two different sagittal slices of a 3D Turbo RARE-scan show the kinetics of inflammatory cell migration (^{19}F MRI) over a period of 6 days in different CNS and lymphatic regions (^{1}H MRI). *In vivo* ^{1}H sequence (as above) and ^{19}F MRI sequence: TR = 800 ms, TE = 6 ms, FOV = (40 × 16 × 16) mm³, Matrix = 100 × 40 × 40, zero fill acceleration 2, RARE Factor = 40, NEX = 256 (scan time = 68 min). (B) Distribution of inflammatory cells (specifically CD3^{+}, CD4^{+}, F4-80^{+} and Mac-2^{+}cells) in EAE tissue that gave a strong ^{19}F signal in MRI. Shown in coronal sections of the cerebellum are specific cell populations (green) and their corresponding uptake of ^{19}F-DiI nanoparticles (red). Arrows indicate colocalization (yellow) of signal from specific immune cell markers (green) and ^{19}F-DiI nanoparticles (red).

We next wanted to study the distribution of distinct immune cell populations in these areas of inflammation. Thus, we fluorescently tagged the ^{19}F nanoparticles for follow up in post fixation experiments and employed the same *in vivo* [19]F/^{1}H MR protocol as above. The ^{19}F nanoparticles were tagged with DiI as fluorescent marker but the ^{19}F content (5 µmoles PFCE per injection) and size (Z-Average Diam. = 170 nm) was kept constant. Following visualization of ^{19}F signal by ^{19}F/^{1}H MRI, we extracted CNS and performed immuno-histological staining for macrophages and lymphocytes in CNS regions where the ^{19}F signal was predominant, specifically cerebellum (**Figure 6B**). We observed a main co-localization of DiI-labeled ^{19}F nanoparticles with F4-80[+] and Mac-2^{+}cells, indicating that the ^{19}F–DiI nanoparticles are primarily taken up by macrophage-like cells from the periphery into the CNS. However we also observed a co-localization of ^{19}F–DiI with CD4^{+} T cells in the cerebellum (**Figure 6B**). We also performed FACS of the CNS tissue and secondary lymphoid organs. As expected, we observed a large percentage of CD3^{+} T cells, CD19^{+} B cells as well as CD11c^{+} and CD11b^{+} myeloid cells in the CNS; most of the latter CD11c^{+} and CD11b^{+} cells were sequestered from the draining lymph nodes (**Supplementary Figure 2** *left panel: no DiI-labeled 19F nanoparticles*). Also with FACS, we observed that CD11c^{+} (30%) and CD11b^{+} (42%) myeloid cells are the predominant immune cells types that transport the ^{19}F–DiI nanoparticles in the CNS (**Supplementary Figure 2**, *right panel: DiI-labeled 19F nanoparticles*). Interestingly, CD3^{+} T cells and CD19^{+} B cells, although present in large quantities, take up a small amount of the ^{19}F–DiI nanoparticles in the CNS and therefore do not contribute significantly to the ^{19}F MR signal we observe in the CNS *in vivo*. In contrast 7% of CD3^{+} T cells and 41% of CD19^{+} B cells were labeled with ^{19}F–DiI nanoparticles in the draining lymph nodes and therefore appear to contribute to the ^{19}F MR signal we observed in the lymph nodes *in vivo*. More detailed *ex vivo* and *in vivo* longitudinal studies will help further identify the rich dynamics of the different immune cell populations that serve as communicating envoys between immune system and CNS during encephalomyelitis.

Discussion

The main motivation for constructing the dual-tunable ^{19}F/^{1}H RF birdcage probe for brain imaging was to increase the sensitivity required to non-invasively follow immune cells in the CNS during inflammation with MRI. The potential applications for ^{19}F in MRI and MR spectroscopy (MRS) have long been recognized[15,16]. The possibility of employing ^{19}F MRI for tracking cells *in vivo* was however first implemented in the last decade. At present, nanoparticles rich in ^{19}F atoms are employed to study immune cell or stem cell migration *in vivo* with the help of ^{19}F/^{1}H MRI[17–22]. However, major challenges particularly signal sensitivity constraints exist. In the present study we prepared nanoparticles (160–170 nm range) from perfluoro-15-crown-5-ether (PFCE) and labeled them with a fluorescent dye (DiI) prior to systemic administration in EAE mice. Thereafter we followed the uptake of the particles by immune cells during the course of the CNS inflammation using the constructed dual-tunable ^{19}F/^{1}H birdcage RF head probe.

The geometry chosen for the present ^{19}F/^{1}H RF probe was very favorable to boost transmission field homogeneity (B_1^+). Indeed, we showed very encouraging results for mouse neuroimaging. One of the benefits of the highly homogenous transmission field was the significant signal improvement in ventral regions of the CNS, particularly in the brain stem and spinal cord, as well as the draining lymph nodes. These areas are otherwise not easily accessible by conventional commercially-available RF head probes (such as small surface coils or phased-array coils) due to depth penetration constraints. The high degree of cylindrical symmetry as well as the absence of chip capacitors also prevented the manifestation of susceptibility artifacts[23]. The elimination of chip capacitors – as improvement to

the original birdcage probe designs – was introduced with the millipede probes[10]. One main advantage of the present 32-leg birdcage probe over the millipede probe is the lower number of legs required due to the shingled design, which makes multiple tuning possible. With the constructed RF probe we achieved a uniform B_1^+ field almost identical for both ^{19}F and ^{1}H channels (3.5% difference in the maximum B_1^+ between both channels in favor of the ^{19}F-channel). The simulations of the ^{1}H channel for the ^{19}F/^{1}H dual-tunable resonator were similar to the ones for a single-tuned ^{1}H linear birdcage resonator with the same dimension. The homogeneous field was indispensable to perform spin echo imaging that is sensitive to changes in power and fluctuations in the B_1^+ field[13,14].

From an RF engineering point of view, the quality of the constructed birdcage probe showed a SNR gain with respect to other coil designs with larger diameters and fewer legs, including those for ^{19}F/^{1}H mouse body imaging (32 mm diameter, 16 legs)[21] in our lab. The electrical measurements – specifically S Parameters – give a quantitative assessment of the quality of the probe. Probes with a high Q Factor have an improved SNR, considering that $SNR \propto \sqrt{Q}$[9,24]. The Q Factor for the unloaded probe (Q_U) was measured to be 130 and when loaded (Q_L) it was 80 – 110. It should be noted that Q_U decreases with increasing number of legs in a birdcage probe[25]. The Q_{ratio} (Q_L/Q_U) gives an indication of the noise dominance, whether it is from the sample or the probe. It should be ideally smaller than 0.5 in order to achieve predominantly sample noise. However, small probes usually have an increased Q_{ratio} since size is inversely proportional to inductance (L) and directly proportional to resistance (R), according to the formula $Q = (w_0 \cdot L)/R$ (ω_0 = resonance frequency)[26,27]. The Q_{ratio} for the constructed 32 leg probe was calculated to be 0.6 – 0.8. Since the noise contribution for our birdcage probe is predominantly probe dependent ($Q_{ratio} > 0.5$), it was imperative to minimize dielectric losses and coil resistance by using low loss PCB material. Furthermore the design of our birdcage probe – in which plate capacitors were built into its structure – reduced resistance by minimizing the soldering connections required for assembling chip capacitors; added soldering also significantly increases resistive losses in small birdcages[25].

The similarity between ^{19}F and ^{1}H NMR properties is an advantage since the same pulse power settings can be used for both nuclei. After power calibration and adjustments for the ^{1}H channel, the same settings can be applied for the ^{19}F channel. For our birdcage probe we altered the overlapping areas between the copper legs to achieve both frequencies. To fine tune to the [1]H (400 MHz) and [19]F (376 MHz) frequencies the reflection coefficient for both frequencies needed to be tweaked by altering the distance of the RF shield to the probe. We used a shield diameter of 48 mm to achieve the best results. According to a previous study investigating the shielding effect on field homogeneity, the ratio between diameter$_{shield}$ and diameter$_{coil}$ should be between 2 and 3; if the shield is closer (ratio < 2) the RF field is disrupted[26]. For the present setup the ratio between diameter$_{shield}$ and diameter$_{coil}$ was 2.4 for the measurements and final simulations. Indeed the B_1^+ field distributions were homogenous across the cross section of the phantom for both simulations and measurements. The deviation of the measured B_1^+ field over the center slice was calculated to be in the range of 6 – 7%, which made this birdcage particularly suitable for 3D fast spin-echo sequences such as RARE since these are more susceptible to B_1^+ field inhomogeneities than gradient echo sequences. A variation in flip angle of less than 10% has no significant influence on spin echo sequences[13,14].

A recognized limitation with our coil design is that the birdcage cannot be driven in quadrature and dual-tunable mode at the same time. Compared to a linear driven birdcage, a quadrature driven coil would add another 41% to SNR gain or reduce the acquisition time to 50% at no cost to SNR. Due to the small size of the coil and space constraints, it is not possible for us (at the current stage) to construct the birdcage in dual-tunable and quadrature driven mode, as has

been shown for human application[28]. Another problem with the quadrature driven mode is the decoupling of the two channels. Potential improvements are to make each channel dual-resonant[29] or to make use of alternate-tuned birdcage elements[11]. Since the proposed design exploits the similarity of proton and fluorine nuclei it might not be possible to apply this technology to low-gamma nuclei.

By using fluorescently-labeled ^{19}F-rich particles we could selectively detect inflammatory cells with ^{19}F/^{1}H MRI and then identify the cell types with the help of fluorescent methods, namely confocal microscopy and flow cytometry. Although the spatial resolution for ^{19}F/^{1}H MRI (μm-range) is not comparable with the high resolution that can be achieved with microscopy (nm-range), it is still possible to study the nature of immune cell infiltration with this technique. Furthermore these experiments can also be done *in vivo* and over a longer period of time; due to the non-invasiveness of the technique it is possible to monitor the migration of immune cells for several days without the necessity of sacrificing the mouse after investigation.

From our study, we could conclude that $CD11c^+$ and $CD11b^+$ myeloid cells are sequestered from the draining lymph nodes (LN) during early stages of the disease to enter the CNS, predominantly into cerebellum, brain stem and also cerebral cortex. The initial ^{19}F signals detected *in vivo* were mostly located within draining LN; typically the submandibular LN, superficial and deeper cervical LN, facial LN and internal jugular LN. These results further support the significance of the lymphatic system for initiation of CNS inflammation. While the role of the draining lymphatic system on priming immune cells to target the CNS has long been known[30], the kinetics of lymphatic drainage in and out of the CNS is still unclear. In this study we start to uncover some of these dynamics between immune system and CNS with the help of ^{19}F/^{1}H MRI. Further elaborate studies need to be undertaken to study the movement of immune cells into the CNS during encephalomyelitis. While it is appealing to employ ^{19}F/^{1}H MRI to study the impact of the immune system on the development of CNS injury during autoimmune encephalomyelitis, it would be also very interesting to employ ^{19}F/^{1}H MRI to study the impact of neuronal damage or degeneration on the outcome of lymphatic drainage. Recently, light has been shed upon the route taken – namely the cribriform plate– by myeloid cells from the site of neuronal injury to the draining cervical LN[31]. These results favor the application of *in vivo* non-invasive approaches such as ^{19}F/^{1}H MRI to monitor the trafficking of immune cells real-time after traumatic injury[32].

In summary, we developed a birdcage RF probe for ^{19}F/^{1}H neuroimaging with a design that promotes signal to noise ratio, a symmetrical cylindrical geometry, a high filling factor and a homogeneous B_1^+-transmit field. The first *in vivo* experiments performed in EAE mice using ^{19}F/^{1}H MRI are promising in that we are in a position to non-invasively follow the kinetics of inflammation specifically due to the near-to-complete absence of ^{19}F in living tissue. Further experiments with ^{19}F/^{1}H MRI in autoimmune encephalomyelitis and also neurodegenerative disorders are warranted to further understand the communication channels between CNS and the immune system.

Methods

Electromagnetic field simulations and probe design. Prior to construction, various probe designs were simulated with Microwave Studio (MWS) (CST, Darmstadt; Germany) and Penn State Birdcage Builder (BB)[33]. After analysis of the EMF simulation results, a 32-leg low pass (LP) probe design was chosen. The details and dimensions for the simulation were chosen as close as possible to the desired birdcage size: diameter = 18.4 mm, total length = 39 mm, leg width = 1 mm, leg length = 33 mm, end ring width = 3 mm, RF shield diameter = 58 mm. Since the capacitance values required for the construction estimated from Birdcage Builder were very small (e.g. for [1]H (400 MHz) C = 1.17 pF), it was not possible to design such a birdcage using chip capacitors. Thus we chose to build the capacitors into the structure of the RF probe by preparing copper strips milled on either side of a double sided copper clad PCB (printed circuit-board) with an area of overlap in between. Figure 1A shows a sketch of the 32-leg ^{19}F/^{1}H LP birdcage design, which was then simulated in MWS.

On each side of the PCB, copper strips were arranged in a way to overlap only a few mm depending on the capacitance and thus frequency required. The long inner copper strips (shown in black) overlap with the outer peripheral copper strips (shown in white) that are connected together by the end rings. We first calculated the overlap required to achieve a basic birdcage frequency (birdcage mode) of 388 MHz (frequency midway between the ^{19}F and ^{1}H frequency). According to the Birdcage Builder this basic frequency necessitates a capacitance of 1.38 pF. To calculate the area of overlap between the strips required in order to achieve the necessary capacitance (C), we used the formula for plate capacitors:

$$C = \varepsilon_0 \cdot \varepsilon_r \cdot A / d$$

where ε_0 = vacuum permittivity constant (8.85418×10^{-12} F/m), A = area of overlap, d = thickness of the PCB that corresponds to the distance between the overlapping strips. For the ensuing probe construction we opted for a special flexible PCB with a high relative permittivity ($\varepsilon_r \approx 10$) and a thickness of 400 μm. Using these values, a capacitance of 0.22 pF is achieved per mm^2 overlap. For the basic frequency of 388 MHz (1.38 pF), we calculated an overlapping area of 6.27 mm^2 and applied this for 28 strips. We then degenerated the basic frequency mode symmetrically to achieve the desired ^{1}H and ^{19}F modes. For the ^{1}H mode, 2 strips were overlapped by an area of 3.14 mm^2 to tune to 400 MHz and for the ^{19}F mode, 2 strips were overlapped by an area of 9.39 mm^2 to tune to 376 MHz. Figure 1B shows a circuit diagram displaying the distribution of all capacitors built into the structure of the RF probe and the corresponding ports.

To construct the 32-leg LP head RF probe, we employed a CNC (computer numerical control) machine Protomat S100 (LPKF, Garbsen, Germany) to mill the 32 copper strips on the PCB cladded with 18 μm copper on both sides (thickness = 400 μm; Taconic CER-10). The PCB is made of low loss material (dissipation factor at 400 MHz tanδ = 0.0025) and has a high permittivity ($\varepsilon_r \approx 10$). Relying on the simulations and calculations, 28 strips were overlapped by 6.27 mm^2 to achieve a capacitance of 1.38 pF and therefore a basic frequency of 388 MHz. For the ^{1}H mode (port 1, marked with * in **Figure 1A**) the overlap was reduced by 3.13 mm^2 to 3.14 mm^2 (C1 = 0.69pF) and for the ^{19}F mode (port 2, marked with **) the overlap was increased by 3.12 mm^2 to 9.39 mm^2 (C2 = 2.08 pF). For fine-tuning the shield diameter was reduced stepwise from 58 mm to 48 mm. Furthermore for load-dependent tuning (C1t and C2t) and matching (C1m and C2m) four small trimmer-capacitors (1-10pF) were used. Figure 2A shows the constructed birdcage RF probe. The dimensions of the RF probe are as follows: outer diameter = 20.42 mm; inner diameter of head probe = 16 mm, total length = 43.29 mm, width of each strip = 1.11 mm, length of each leg = 36.63 mm, width of end rings = 3.33 mm, diameter of RF shield (not shown) = 48 mm. All parts for the housing of the 32-leg LP head RF probe were designed using Autodesk Inventor 2011 (Autodesk Inc., San Rafael, CA, USA) and built with a 3D Printer BST 1200es (Dimension Inc., Eden Prairie, MN, USA). The RF performance of the head RF probe – including the measurement of the full set of scattering parameters (S-parameter) that determine the reflection coefficients as well as coupling between the two ports (**Figure 1D**) – was tested with a 2channel vector network analyzer (Rhode & Schwarz GmbH & Co. KG, Memmingen, Germany).

To block unwanted coaxial shield currents, we used baluns on each channel connected as close as possible to the birdcage probe. The baluns were built from semi-rigid cable (diameter 1.5 mm), bent into a loop with a radius of 7.5 mm and soldered on a small piece of printed circuit board. Two 3 mm chip capacitors in the range of 2.2 pF–2.7 pF were used to tune the baluns to 376 MHz and 400 MHz.

B_1^+ **simulations and measurements.** For B_1^+ simulations we applied a 3D model using MWS (**Figure 2A**) in which a 15-ml Falcon tube (conductivity: σ = 0.33 S/m, relative permittivity: ε = 78) was used as phantom for loading the RF probe; we simulated the load an average mouse head would add to the probe. The transmit-active component (B_1^+) of RF probes can be measured by several flip-angle mapping techniques[34]. For B_1^+ measurements, the probe was loaded with a 15 ml tube filled with saline solution doped with $CuSO_4$ (0.3 g/L) to decrease the T_1 relaxation time to c. 600 ms. This diminishes T_1 related effects and thus reduces measurement time. For the phantom measurements, we applied a time-consuming but simple and accurate technique based on a set of rectangular non-selective preparation pulses (pulse length = 1 ms) followed by spoiler gradients to destroy any transversal magnetization[35]. This way a 3D distribution of longitudinal magnetization (M_z) was produced for the whole volume of interest with 7 different power settings for the preparation pulses. After each preparation step, the M_z-distribution of a central slice was mapped, using a standard 2D gradient-echo sequence with a small flip-angle and long TR (TR min. $5 \cdot T_1 = 3$ s) to avoid T_1-related effects: TR = 3000 ms, TE = 6 ms, slice thickness 1 mm, FOV = (15 × 15) mm^2, Matrix 64 × 64, NEX = 1, 7 preparation pulses (attenuators = 150 dB, 56.4 dB, 44.4 dB, 39.5 dB, 36.4 dB, 32.3 dB, 31.3 dB), scan time = 35 min.

Preparation of ^{19}F-rich DiI-labeled nanoparticles. For the ensuing *in vivo* [19]F/^{1}H MRI in EAE mice and post fixation experiments (histology and flow cytometry), we prepared nanoparticles with high fluorine (^{19}F) content and DiI fluorescence, respectively. These particles consisted of 600 mM perfluoro-15-crown-5-ether (PFCE, Fluorochem, Derbyshire, UK) and 630 μM 1,1'-Dioctadecyl-3,3,3',3'-Tetramethyl, indocarbocyanine Perchlorate (DiI, Molecular Probes®, Invitrogen, Darmstadt, Germany) and were prepared by first emulsifying PFCE in Pluronic F-68 (Sigma-Aldrich, Germany) via direct sonication, using a cell disrupting titanium sonotrode (Bandelin Sonopuls GM70, Bandelin, Berlin, Germany) as previously

described[21]. After 1 : 1 (v/v) dilution with DPBS, the PFCE emulsion was further sonicated in the presence of 630 μM DiI to obtain a PFCE-DiI nanoparticle emulsion containing 600 mM PFCE. In order to remove free DiI, the PFCE-DiI nanoparticle emulsion was then clarified on Sephadex G-50 (Sigma-Aldrich, Germany) columns. The average nanoparticle diameter was determined by dynamic light scattering using a Malvern Zetasizer Nano ZS instrument (Malvern Instruments, Worcestershire, UK). The particle size remained constant after incorporation of the DiI.

In vitro experiments. To determine the uptake capacity for the prepared particles, and optimize the ^{19}F and DiI content, we labeled bone marrow derived dendritic cells (BMDC) with the PFCE-DiI nanoparticles. BMDC were prepared from BM suspensions as previously described[36]. Briefly, BM from femurs of C57BL/6 mice were grown in RPMI-1640 medium containing 10% FCS (Biochrom, Germany) and supplemented with 100 ng/ml of GM-CSF.

In vivo experiments. Animal experiments were carried out in accordance to guidelines provided and approved by the Animal Welfare Department of the State Office of Health and Social Affairs Berlin (*LAGeSo*). For active EAE, female SJL/J mice (Janvier SAS, Le Genest-St-Isle, France) were immunized subcutaneously with 250 μg PLP$_{139-151}$ purity >95% (Pepceuticals Ltd., UK) together with Complete Freund's Adjuvant and heat-killed Mycobacterium tuberculosis (H37Ra, Difco). Bordetella pertussis toxin (250 ng; List Biological Laboratories, US) was administered intraperitoneally at days 0 and 2. On each day following immunization mice were weighed and scored as follows: 0, no disease; 1, tail weakness and righting reflex weakness; 2, paraparesis; 3, paraplegia; 4, paraplegia with forelimb weakness or paralysis; 5, moribund or dead animal. Five days following EAE induction, mice were administered with DiI-labeled nanoparticles containing 5 μmol PFCE.

For ^{19}F/^{1}H MRI, EAE mice were anesthetized using a mixture of isofluoranes inhalation narcosis (0.5–1.5%), pressurized air and oxygen shortly before and during the MR session. The mice were positioned prone on the mouse holder of a small animal MR scanner (Bruker Biospin USR 94/20, Bruker Biospin, Ettlingen, Germany) with the head inside the ^{1}H/^{19}F RF probe which was then moved to the isocenter of the magnet. Following acquisition of scout images using 2D FLASH (MRI Software Paravision 5.1, Bruker Biospin, Ettlingen, Germany), the RF head probe was tuned to both ^{1}H and ^{19}F resonance frequency and then matched to the characteristic impedance (50 Ohm) using the tuning monitor of the animal MR scanner. Following automatic system settings including 1st and 2nd order shimming to fine-tune the homogeneity of the magnetic field, we employed a TurboRARE 3D sequence for ^{1}H: TR = 1500 ms, TE = 53 ms, FOV = (40 × 16 × 16) mm^3, Matrix = 320 × 128 × 128, RARE Factor = 16, NEX = 1 (scan time ca. 25 min); for ^{19}F: TR = 1000 ms, TE = 6 ms, FOV = (40 × 16 × 16) mm^3, Matrix = 100 × 40 × 40, zero fill acceleration 2, RARE Factor = 40, NEX = 128 (scan time = 45 min). For overview scans and serving as a reference to the ^{19}F MRS, we used a 2D FLASH protocol for ^{19}F: TR = 15 ms, TE = 3.3 ms, one sagittol 3 mm slice, in-plane resolution (400 × 400) μm^2, NEX = 2048 (scan time = 15 min) and for ^{1}H: TR = 473 ms, TE = 13 ms, 22 slices, inplane resolution (73 × 73) μm^2, NEX = 16 (scan time = 25 min).

For quantification of the ^{19}F content in specified regions of the mouse brain, we employed single voxel spectroscopy (SVS), in particular Point RESolved Spectroscopy (PRESS). For this purpose we placed a (3 × 3 × 3) mm^3 voxel within the region of interest (here cerebellum and cortex) of the mouse-brain (Figure 4). Then we employed the FastMap[37] method from Paravision, for volume specific magnetic field (B$_0$) shimming. After shimming the spectra where acquired using a PRESS-protocol for ^{19}F MRS: TR = 1500 ms, TE = 11.6 ms, voxelsize (3 × 3 × 3) mm^3, NEX512 (scan time = 13 min). To quantify the ^{19}F signal we acquired a ^{19}F MRS calibration curve using the same PRESS protocol with three 15 ml Falcon tubes containing different concentrations of our PFCE Emulsion (10, 20 and 40 mM).

Post fixation experiments. For histological and immunohistochemistry investigations, EAE mice were transcardially perfused with 20 ml cold PBS following terminal anesthesia. Thereafter, perfusion was continued with 20 ml cold PFA (4% in PBS). Brain, spinal cord and secondary lymphoid organs were then extracted and subsequently post-fixed overnight in 4% PFA at 4°C. The tissue was then cryoprotected with sucrose (30% in PBS) at 4°C, sectioned in 50 μm thick slices on a cryostat at −20°C and processed on the same day. Free floating sections were washed and incubated with antibodies against Mac2 (ACRIS GmbH, Herford, Germany), CD4 (BD Pharmingen, Heidelberg, Germany), CD3 (Serotec, Düsseldorf, Germany), F4-80 (Biolegend, Fell, Germany) and MPO (Abcam, Cambridge, UK) overnight at 4°C, thereafter washed in PBS and incubated with secondary antibodies conjugated with Cy3 (Jackson, West Grove, Pennsylvania, USA) for 2 h at room temperature. Some sections were incubated with FITC-conjugated B220 (Biolegend, Fell, Germany). After antibody incubations, sections were mounted on standard glass slides and covered with Vectashield-DAPI (Vector Laboratories, Burlingame, California, USA) for fluorescence microscopy. Microphotographs were acquired using a fluorescence microscope (BZ-9000, Keyence, Neu-Isenburg, Germany).

For *flow cytometry* (FACS) experiments, mice were transcardially perfused with 20 ml cold PBS following terminal anesthesia. After extraction, organs (brain, spinal cord, lymph nodes, spleen) were mechanically dissociated through a 70 μm nylon cell strainer (BD Falcon, Heidelberg, Germany) into RPMI medium (containing 5% FCS) and centrifuged at 4°C. To remove contaminating erythrocytes from the dissociated tissue, a lysis buffer was employed. For the CNS, cells were separated from myelin and debris using a 37% Percoll gradient (1.125–1.135 g/ml; Sigma-Aldrich, Germany). The resulting cells were incubated with anti-CD16/32 Fc-receptor block (BD

Pharmingen™, Heidelberg, Germany) for 15 min, washed in FACS buffer and prepared for FACS surface staining with APC-conjugated CD3, FITC-conjugated CD19, Pacific Blue-conjugated CD11b and APC-conjugated CD11c antibodies (eBioscience, Frankfurt, Germany).

For *electron microscopy*, mice underwent terminal anesthesia and were transcardially perfused with 4% formaldehyde and 0.5% glutaraldehyde prior to brain extraction. A 3 mm^3 cube (enclosing the PRESS-voxel used for spectroscopy) was dissected from cerebellum and post-fixed (for 24 h in 2% gluteraldehyde, thereafter for 4 h in 1% osmium tetroxide). Following dehydration, tissue was embedded in Poly/Bed 812 (Polysciences, Eppelheim, Germany). Semithin sections were stained with toluidine blue and ultrathin sections were stained with uranyl acetate/lead citrate. Sections were imaged using a FEI Morgagni electron microscope (FEI, Eindhoven, NL) and the iTEM software (Olympus-SIS, Münster, Germany).

1. Charil, A. & Filippi, M. Inflammatory demyelination and neurodegeneration in early multiple sclerosis. *J. Neurol. Sci.* **259**, 7–15 (2007).
2. Trapp, B. D. & Nave, K.-A. Multiple sclerosis: an immune or neurodegenerative disorder? *Annu. Rev. Neurosci.* **31**, 247–69 (2008).
3. Stadelmann, C. Multiple sclerosis as a neurodegenerative disease: pathology, mechanisms and therapeutic implications. *Curr. Opin. Neurol.* **24**, 224–9 (2011).
4. Dousset, V., Gomez, C., Petry, K. G., Delalande, C. & Caille, J. M. Dose and scanning delay using USPIO for central nervous system macrophage imaging. *Magma* **8**, 185–9 (1999).
5. Floris, S. *et al.* Blood-brain barrier permeability and monocyte infiltration in experimental allergic encephalomyelitis: a quantitative MRI study. *Brain* **127**, 616–27 (2004).
6. Tysiak, E. *et al.* Beyond blood brain barrier breakdown – in vivo detection of occult neuroinflammatory foci by magnetic nanoparticles in high field MRI. *J. Neuroinflamm.* **6**, 20 (2009).
7. Oude Engberink, R. D. *et al.* Dynamics and fate of USPIO in the central nervous system in experimental autoimmune encephalomyelitis. *NMR Biomed.* **23**, 1087–96 (2010).
8. Ruiz-Cabello, J., Barnett, B. P., Bottomley, P. a. & Bulte, J. W. M. Fluorine ((19)F) MRS and MRI in biomedicine. *NMR Biomed.* (2010).
9. Hoult, D. & Richards, R. The signal-to-noise ratio of the nuclear magnetic resonance experiment. *J. Magn. Reson.* **24**, 71–85 (1976).
10. Wong Ernest, W. H. Millipede Coils. *Encycl. Magn. Reson.* (2007).
11. Tomanek, B., Volotovskyy, V., Gruwel, M. L. H., McKenzie, E. & King, S. B. Double-frequency birdcage volume coils for 4.7T and 7T. *Concept. Magn. Reson. B* **26B**, 16–22 (2005).
12. Waiczies, H. *et al.* Identification of Cellular Infiltrates during Early Stages of Brain Inflammation with Magnetic Resonance Microscopy. *PLoS ONE* **7**, e32796 (2012).
13. Hornak, J. P., Szumowski, J. & Bryant, R. G. Magnetic field mapping. *Magn. Reson. Med.* **6**, 158–63 (1988).
14. Dowell, N. G. & Tofts, P. S. Fast, accurate, and precise mapping of the RF field in vivo using the 180 degrees signal null. *Magn. Reson. Med.* **58**, 622–30 (2007).
15. Holland, G. N. & Hinshaw, P. A. B. W. S. Communications 19F Magnetic Resonance Imaging. *J. Magn. Reson.* **136**, 133–136 (1977).
16. Liu, M. S. & Long, D. M. Perfluoroctylbromide as a diagnostic contrast medium in gastroenterography. *Radiology* **122**, 71–6 (1977).
17. Ahrens, E. T., Flores, R., Xu, H. & Morel, P. a In vivo imaging platform for tracking immunotherapeutic cells. *Nat. Biotechnol.* **23**, 983–7 (2005).
18. Srinivas, M., Morel, P. a., Ernst, L. A., Laidlaw, D. H. & Ahrens, E. T. Fluorine-19 MRI for visualization and quantification of cell migration in a diabetes model. *Magn. Reson. Med.* **58**, 725–34 (2007).
19. Partlow, K. C. *et al.* 19F magnetic resonance imaging for stem/progenitor cell tracking with multiple unique perfluorocarbon nanobeacons. *FASEB J.* **21**, 1647–54 (2007).
20. Srinivas, M. *et al.* In vivo cytometry of antigen-specific t cells using 19F MRI. *Magn. Reson. Med.* **62**, 747–53 (2009).
21. Waiczies, H. *et al.* Perfluorocarbon particle size influences magnetic resonance signal and immunological properties of dendritic cells. *PloS one* **6**, e21981 (2011).
22. Srinivas, M., Boehm-Sturm, P., Figdor, C. G., De Vries, I. J. & Hoehn, M. Labeling cells for in vivo tracking using 19F MRI. *Biomaterials* (2012).
23. Doty, F. D., Entzminger, G., Kulkarni, J., Pamarthy, K. & Staab, J. P. Radio frequency coil technology for small-animal MRI. *NMR Biomed.* **20**, 304–25 (2007).
24. Hill, H. D. W. & Richards, R. E. Limits of measurement in magnetic resonance. *J. Phys. E Sci. Instrum.* **1**, 977–983 (1968).
25. Crozier, S., Luescher, K., Forbes, L. K. & Doddrell, D. M. Optimized Small-Bore, High-Pass Resonator Designs. *Magn. Reson. Med., Series B* **109**, 1–11 (1995).
26. Mispelter, J. & Lupu, M. Homogeneous resonators for magnetic resonance: A review. *C. R. Chim.* **11**, 340–355 (2008).
27. Giovannetti, G., Hartwig, V., Landini, L. & Santarelli, M. F. Low-Field MR Coils: Comparison between Strip and Wire Conductors. *Appl. Magn. Reson.* **39**, 391–399 (2010).
28. Shen, G. X., Wu, J. F., Boada, F. E. & Thulborn, K. R. Experimentally verified, theoretical design of dual-tuned, low-pass birdcage radiofrequency resonators for magnetic resonance imaging and magnetic resonance spectroscopy of human brain at 3.0 Tesla. *Magn. Reson. Med.* **41**, 268–75 (1999).

29. Hu, L. *et al.* A generalized strategy for designing (19)F/(1)H dual-frequency MRI coil for small animal imaging at 4.7 Tesla. *J. Magn. Reson. Im.* **34**, 245–52 (2011).
30. Phillips, M. J., Needham, M. & Weller, R. O. Role of cervical lymph nodes in autoimmune encephalomyelitis in the Lewis rat. *J. Pathol.* **182**, 457–64 (1997).
31. Kaminski, M. *et al.* Migration of monocytes after intracerebral injection at entorhinal cortex lesion site. *J. Leukocyte. Biol.* **92**, 31–9 (2012).
32. Laman, J. D. & Weller, R. O. Editorial: route by which monocytes leave the brain is revealed. *J. Leukocyte. Biol.* **92**, 6–9 (2012).
33. Chin, C.-L., Collins, C. M., Li, S., Dardzinski, B. J. & Smith, M. B. BirdcageBuilder: Design of specified-geometry birdcage coils with desired current pattern and resonant frequency. *Concept. Magnetic. Res.* **15**, 156–163 (2002).
34. Jiru, F. & Klose, U. Fast 3D radiofrequency field mapping using echo-planar imaging. *Magn. Reson. Med.* **56**, 1375–9 (2006).
35. Seifert, F., Wübbeler, G., Junge, S., Ittermann, B. & Rinneberg, H. Patient safety concept for multichannel transmit coils. *J. Magn. Reson. Im.* **26**, 1315–21 (2007).
36. Bendix, I. *et al.* MAPK3 deficiency drives autoimmunity via DC arming. *Eur. J. Immunol.* **40**, 1486–95 (2010).
37. Gruetter, R. Automatic, localizedin Vivo adjustment of all first-and second-order shim coils. *Magn. Reson. Med.* **29**, 804–811 (1993).

Author contributions

H.W., T.N. and S.W. conceived and designed the study. H.W., S.L., F.Q., B.P., A.P. and S.W. carried out the experiments and measurements. HW and WH developed the RF-Probe. A.K. and T.L. helped with EMF simulations and B_1^+- mapping. S.D., S.W., K.S. and M.D. developed the ^{19}F/DiI-nanoparticles. S.W., H.W. and T.N. wrote the manuscript with the assistance of all other co-authors.

Additional information

Supplementary information accompanies this paper at http://www.nature.com/scientificreports

Competing financial interests: The authors declare no competing financial interests.

How to cite this article: Waiczies, H. *et al.* Visualizing Brain Inflammation with a Shingled-Leg Radio-Frequency Head Probe for ^{19}F/^{1}H MRI. *Sci. Rep.* **3**, 1280; DOI:10.1038/srep01280 (2013).